

PAPER • OPEN ACCESS

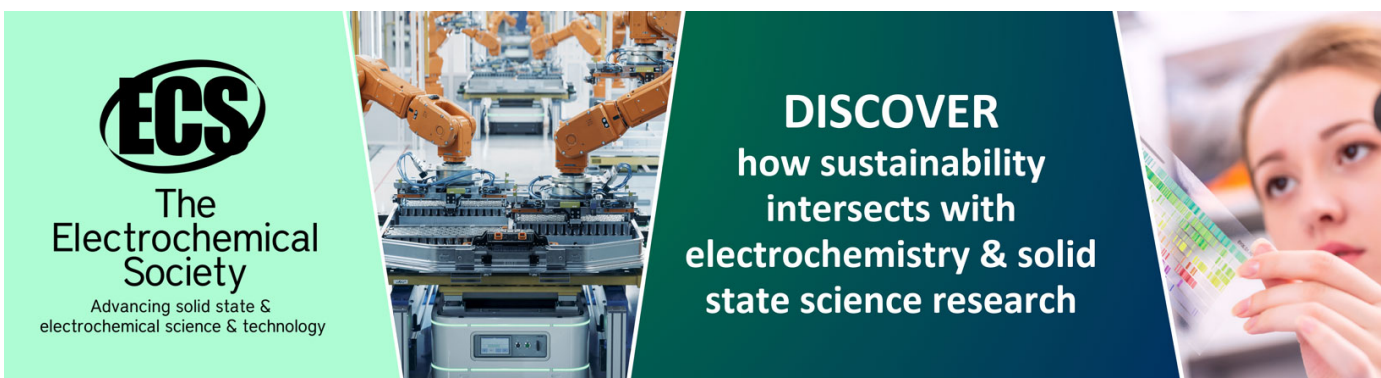
Design of a Talbot phase-contrast microscopy imaging system with a digital detector for laser-driven X-ray backlighter sources

To cite this article: S. Schreiner *et al* 2024 *JINST* **19** P05004

View the [article online](#) for updates and enhancements.

You may also like

- [Development of a PET/EPRI combined imaging system for assessing tumor hypoxia](#)
H. Kim, B. Epel, S. Sundramoorthy et al.
- [Development of High Throughput Single-Cell Analysis System for Circulating Tumor Cells Based on Digital Micromirror Device](#)
Ryo Negishi, Hyuga Saito, Tsuyoshi Tanaka et al.
- [H and H Absorption-line Profile Inconsistencies in Laboratory Experiments Performed at White Dwarf Photosphere Conditions](#)
M.-A. Schaeuble, T. Nagayama, J. E. Bailey et al.



ECS
The
Electrochemical
Society
Advancing solid state &
electrochemical science & technology

DISCOVER
how sustainability
intersects with
electrochemistry & solid
state science research

Design of a Talbot phase-contrast microscopy imaging system with a digital detector for laser-driven X-ray backlighter sources

S. Schreiner¹,^{a,*} C. Rauch¹,^a B. Akstaller¹,^a P. Bleuel¹,^a E. Fröjdh¹,^c V. Ludwig¹,^a A. S. Martynenko¹,^b P. Meyer¹,^d A. Mozzanica¹,^c M. Müller,^a P. Neumayer,^b M. Schuster¹,^a L. Wegert¹,^b B. Zielbauer,^b A. Wolf¹,^a G. Anton¹,^a T. Michel¹,^a and S. Funk¹,^a

^aErlangen Centre for Astroparticle Physics (ECAP), Friedrich-Alexander Universität Erlangen-Nürnberg, Nikolaus-Fiebiger-Straße 2, Erlangen 91058, Germany

^bGSI Helmholtzzentrum für Schwerionenforschung GmbH, Planckstraße 1, Darmstadt 64291, Germany

^cKarlsruhe Institute of Technology, Institute of Microstructure Technology, Hermann-von-Helmholtz-Platz 1, Eggenstein-Leopoldshafen 76344, Germany

^dPaul Scherrer Institut (PSI), Forschungsstrasse 111, Villigen 5232, Switzerland

E-mail: ste.schreiner@fau.de

ABSTRACT: Laser-driven shock waves in matter propagate with multiple kilometers per second and therefore require sources like a laser-driven backlighter, which emit the X-rays within picoseconds, to be able to capture sharp images. The small spatial extent of shocks in low-density materials pose challenges on the imaging setup. In this work, we present a design process for a single-shot X-ray phase-contrast imaging system geared towards these objects, consisting of a two-grating Talbot interferometer and a digital X-ray detector. This imaging system is optimized with respect to the detectable refraction angle of the X-rays induced by an object, which implies a high phase sensitivity. Therefore, an optimization parameter is defined that considers experimental constraints such as the limited number of photons, the required magnification, the size and spectrum of the X-ray source, and the visibility of the moiré fringes. In this way, a large parameter space is sampled and a suitable imaging system is chosen. During a campaign at the PHELIX high-power laser facility a static test sample was imaged which is used to benchmark the optimization process and the imaging system under real conditions. The results show good agreement with the predicted performance, which demonstrates the reliability of the presented design process. Likewise, the process can be adapted to other types of laser experiments or X-ray sources and is not limited to the application presented here.

KEYWORDS: Inspection with x-rays; Models and simulations; Plasma diagnostics - interferometry, spectroscopy and imaging; X-ray radiography and digital radiography (DR)

*Corresponding author.

Contents

1	Introduction	1
2	Methods	2
2.1	Talbot imaging	2
2.2	Phase sensitivity and smallest detectable refraction angle	4
3	Setup design	5
3.1	Detection efficiency and design energy	5
3.2	Imaged sample	7
3.3	Geometric and experimental constraints	8
3.4	Optimization parameter and numerical simulation	9
4	Experimental verification of the design process at the PHELIX laser	13
5	Conclusion and outlook	16

1 Introduction

Compared to imaging based on X-ray absorption contrast, phase-contrast imaging (PCI) exploits the refraction of X-ray [1]. Being sensitive to the refraction of X-ray has the potential to better discriminate low-Z elements or small density contrasts [2]. Consequently, it is being intensively investigated for medical imaging of soft tissues [3–5], as well as non-destructive testing [6, 7]. Currently the propagation-based approach [8] and the grating-based approach [9–13] are investigated for high energy density (HED) experiments.

This paper aims to design a grating interferometer that is capable of acquiring differential phase-contrast images of a laser-driven shock wave in matter at the Petawatt High-Energy Laser for Heavy Ion Experiments (PHELIX) [14] at the GSI Helmholtzzentrum für Schwerionenforschung GmbH. In this scenario, a grating-based approach is favored over propagation-based phase-contrast imaging. First, the limited photon flux from the uniformly emitting X-ray backlighter [15] together with the long propagation distances between source, target, and detector required for the propagation approach [16] causes a high level of photon noise. For the grating-based approach, these strict requirements for long propagation distances do not apply. Furthermore, the grating-based approach is proportional to the first derivative of the phase shift induced by an object, whereas the propagation-based approach is, in the first approximation, sensitive to the second derivative [2]. This implies that the grating-based approach is more sensitive to weak density gradients [2]. Since the induced phase shift is directly proportional to the projected electron density of an object [1], the grating-based approach promises advantages for retrieving the projected electron density, which is of interest in HED science.

Grating-based phase-contrast imaging requires a well-designed setup to obtain high-quality images. One parameter to determine the quality of a grating setup is the contrast of the fringe pattern, which is used for retrieving the differential phase-contrast images. Further, when imaging tiny objects with low density variations, the phase sensitivity is a crucial parameter as well. Unfortunately, both

parameters influence each other, and hence cannot be tuned independently. To account for that, both parameters must be considered when designing the grating interferometer.

There is already a wide variety of publications on the optimization of grating-based phase-contrast imaging systems [17–20]. Most of them investigate a three-grating Talbot-Lau setup [18, 20] that uses the phase-stepping technique [21], as these setups are widely used in medical applications and non-destructive testing. However, these setups usually have completely different X-ray sources and are optimized for other samples, making the procedure hard to adopt. When the focal spot of the X-ray backlighter is small enough and thus provides sufficient spatial coherence, one of the two absorption gratings used in the Talbot-Lau setup can be omitted [22]. This is also the case for X-ray backlighter sources with sufficiently small extent [9]. Omitting one absorption grating significantly increases the photon statistics but also limits the number of possible grating configurations due to source blurring. Single-shot acquisition, which is required to image laser-driven shock waves in matter, makes the moiré imaging technique [23, 24] essential.

In this paper, we present our method of optimizing a two-grating Talbot interferometer with respect to fringe visibility, phase sensitivity, and photon noise for imaging a laser-driven shock wave at a pump-probe experiment. Geometric constraints and requirements of the grating setup are discussed with respect to the expected sample. Data from a previous experiment performed at the PHELIX facility is used as a reference point for optimization. Wave-field simulations are performed to obtain an optimal set of grating parameters. Finally, the designed imaging setup is evaluated with data acquired during a recent experiment at the PHELIX laser facility.

2 Methods

2.1 Talbot imaging

Phase-contrast imaging allows to extend standard absorption-based imaging by additionally probing refractive effects to complement standard radiography techniques. Hence, both parts of the complex refractive index $n = 1 - \delta + i\beta$, with δ the refractive index decrement and β the imaginary part [1], can be probed. This is done in this work using Talbot interferometry, also known as Talbot deflectometry or shearing interferometry [21, 25–27]. The optimization presented in this work is based on a two-grating interferometer and a laser-driven X-ray backlighter source [28] in combination with a digital detector. A sketch of this setup is shown in figure 1. A tungsten backlighter ① is irradiated with an intense laser pulse ② and, as a result of the generated plasma, emits a broad X-ray spectrum [15]. To achieve a high magnification, the micro-structured sample ③ is placed close to the backlighter. The phase grating G_1 ⑤ and the absorption grating G_2 ⑥, are placed downstream of the object. The X-rays are finally detected with a pixelated detector ⑦.

Grating-based phase-contrast is based on the Talbot effect [29]. When illuminating a grating with a spatially coherent X-ray source, self-images of the grating appear downstream of the periodic structure. For absorption gratings with period p , these structures appear after a certain propagation distance, called the Talbot distance, $Z_t = 2p^2/\lambda$. For phase-shifting gratings, self-images occur before the Talbot distance, called fractional Talbot distances [25]. The exact positions depend additionally on the ratio between the grating bar width and the grating period, called the duty cycle (DC), and the phase-shift the grating imprints on the phase front. One specialty for π -shifting gratings is that the self-image has twice the frequency of the G_1 period; an effect referred to as frequency doubling [25].

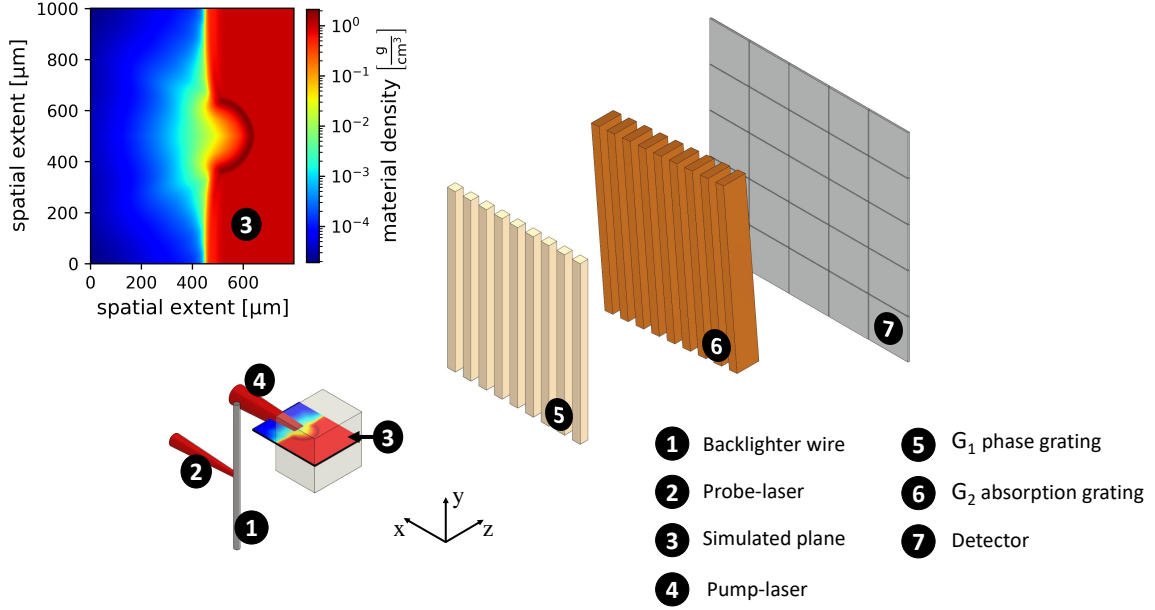


Figure 1. Scheme of a Talbot interferometer with a laser-driven X-ray source. The backlighter wire ① has a diameter of $5\ \mu\text{m}$ and is irradiated with a laser ②. A solid target ③ is hit by another intense laser pulse ④, creating a propagating plasma. The density distribution ③ simulated in a plane of the target is depicted within the target and on the top left in a logarithmic scale. Note that the simulation is radially symmetric around the pump laser propagation direction. The two gratings ⑤ and ⑥ are aligned to each other to form a moiré pattern, which is imaged by the detector ⑦.

If an object is in the beam path, altering the phase front impinging on G_1 , the Talbot pattern is shifted. Hence, the Talbot effect translates a phase shift into a spatially resolvable intensity shift. Unfortunately, the fringe pattern and its spatial shift cannot be detected due to insufficient spatial resolution of common hard X-ray detectors. A second grating, G_2 , is superimposed to overcome this limitation. If the angle and period of the G_2 grating and the magnified Talbot pattern match within small variations, a moiré pattern is formed [30]. This moiré pattern can be tuned to the required periodicity. The information of the phase-shift is then encoded in this enlarged pattern [30]. The contrast of the moiré pattern is called visibility and can be quantified by

$$V = \frac{\tilde{I}_{\max} - \tilde{I}_{\min}}{\tilde{I}_{\max} + \tilde{I}_{\min}}, \quad (2.1)$$

with \tilde{I}_{\max} and \tilde{I}_{\min} the maximum and minimum intensity [1].

Image retrieval for single-shot acquisition is done by comparing two images: a reference image I_{ref} , where no object is present, and an object measurement I_{obj} . The moiré pattern of these images can be written according to Takeda et al. [24] as

$$I(x, y) = A_{x,y} \left(1 + V_{x,y} \sin \left(2\pi/\lambda_m \cdot x + \phi_{x,y} \right) \right), \quad (2.2)$$

with image coordinates x, y , amplitude $A_{x,y}$, the fringe visibility $V_{x,y}$, the phase of the moiré pattern $\phi_{x,y}$ and λ_m the distance between two maxima of the moiré pattern. The analysis is done in Fourier space, since there the high-frequency moiré pattern is separated from the low-frequency object

signatures. Following Takeda et al. [24] with slight modifications introduced by Seifert et al. [31], the parameters $A_{x,y}$, $V_{x,y}$ and $\phi_{x,y}$ can be retrieved individually. The transmission image T , the differential phase image $\Delta\varphi$ and the dark-field image Df are calculated using the following expressions: [23, 32]:

$$T = \frac{A_{\text{obj}}}{A_{\text{ref}}}, \quad \Delta\varphi = \phi_{\text{obj}} - \phi_{\text{ref}}, \quad Df = \frac{V_{\text{obj}}}{V_{\text{ref}}}, \quad (2.3)$$

with the variables A , V and ϕ introduced in equation (2.2). The indices $_{\text{ref}}$ and $_{\text{obj}}$ refer to the reference and the object measurement, respectively. The transmission image T , the standard radiograph, is retrieved by removing the moiré modulation and thus only using the amplitude A . The differential phase-contrast image $\Delta\varphi$ is derived by calculating the difference between the two phases ϕ of the moiré pattern. The dark-field image Df is a measure for the fringe visibility ratio. It indicates small angle scattering of the probing X-rays and occurs at object boundaries and granular or fibrous materials [33]. Dark-field imaging is attractive for probing the micro-structure of objects with macroscopic spatial resolution [34]. But since this publication strives for a quantitative analysis of δ and β , the dark-field will no longer be taken into consideration.

2.2 Phase sensitivity and smallest detectable refraction angle

One major difference between absorption-based imaging and GBPCI is that the differential phase-contrast signal $\Delta\varphi$ of the investigated object is sensitive to the spatial arrangement of the object and the relative alignment of the gratings. According to [21, 22, 35] the differential phase-contrast signal is given by

$$\Delta\varphi = \frac{2\pi \cdot d(G_1, G_2)}{P_{G_2} \cdot M_{(\text{Obj}, G_1)}} \cdot \Delta\alpha_{\text{obj}}(x, y), \quad (2.4)$$

with λ the wavelength of the probing X-rays, $d(G_1, G_2)$, the inter-grating distance, P_{G_2} the period of G_2 , $M_{(\text{Obj}, G_1)}$ the magnification of the object into the G_1 plane and $\Delta\alpha_{\text{obj}}(x, y)$ the angle of refraction induced by an object. The refraction angle $\Delta\alpha_{\text{obj}}(x, y)$ can be calculated in the projection approximation [1] using

$$\Delta\alpha_{\text{obj}}(x, y) = \frac{\partial}{\partial x} \left(\int_0^{z_{\text{obj}}} \delta_{\lambda}^{\text{obj}}(x, y, z) dz \right), \quad (2.5)$$

with $\delta_{\lambda}^{\text{obj}}$ the refraction index of the object material and z_{obj} the thickness of the object sample [1]. The coordinate system matches the one shown in figure 1. Note that equation (2.5) is valid for a monochromatic X-ray source. If a polychromatic source is used, the refraction angle $\Delta\alpha_{\text{obj}}$ will change depending on the X-ray energy, which should be taken into account.

However, equation (2.4) is not suitable for optimization as it does not incorporate noise stemming from the limited photon flux or low visibility. Following [17, 20], a good measure for the overall performance of a grating setup regarding the resolution of the differential phase-contrast signal is the minimum observable refraction angle α_{min} , which is given by

$$\alpha_{\text{min}} = \frac{P_{G_2} \cdot M_{(\text{Obj}, G_1)}}{2\pi \cdot d(G_1, G_2)} \cdot \text{std}(\Delta\varphi), \quad (2.6)$$

with $\text{std}(\Delta\varphi)$, the standard deviation of the differential phase-contrast image $\Delta\varphi$, with no object in the beam path, as a measure of the uncertainty. In this work, $\text{std}(\Delta\varphi)$ is either determined using an area

in the reconstructed differential phase-contrast image where no object is present (free-field), or by following [20, 36, 37] for an analytical expression for an estimator of the noise

$$\text{std}(\Delta\varphi) \propto \frac{\sqrt{2}}{V\sqrt{N_\gamma}}, \quad (2.7)$$

with V the visibility of the fringe pattern and N_γ the mean number of photons per pixel. Note that equation (2.7) is precise for the phase-stepping technique and proportional for the moiré imaging [38]. Equation (2.6) and (2.7) are used in section 3.4 to evaluate the performance of the simulated grating interferometer.

3 Setup design

To optimize the imaging system for laser-driven plasma shocks, it is crucial to take the characteristics of such experiments into account. Since laser-driven plasma shocks typically propagate with multiple kilometers per second [39], an X-ray source with a short emission time is necessary. A laser-driven X-ray backlighter provides such a short flash. However, this source comes with a limited photon flux and a quantitatively unknown spectrum that additionally varies from shot to shot. This makes a purely analytical approach difficult. For this reason, existing data from campaign P186 at the PHELIX laser in 2020 will also be analyzed and incorporated into the design process.

3.1 Detection efficiency and design energy

When imaging with a polychromatic source, it is important to keep in mind that the X-ray transmission through matter, the induced phase shift and the detection efficiency of the detector is highly dependent on the X-ray energy. Thus, a detector image \bar{I} can be calculated using

$$\bar{I} = \sum_i \frac{w(\lambda_i)}{\sum_j w(\lambda_j)} \cdot I_i(\lambda_i), \quad (3.1)$$

with I_i , the i -th raw detector image, simulated with monochromatic X-rays with a wavelength λ_i , and a weighting factor $w(\lambda_i)$. The indices i and j enumerate the simulated X-ray energies. The weighting factor $w(\lambda_i)$ is calculated using

$$w(\lambda_i) = \mathcal{S} \cdot \mathcal{C} \cdot E_\gamma, \quad (3.2)$$

with \mathcal{S} , the spectrum of the X-ray backlighter, \mathcal{C} the detection efficiency and E_γ , the associated photon energy. To optimize the grating setup in the correct X-ray energy range, the weighting factor $w(\lambda_i)$ is determined first.

For X-ray sources, like conventional X-ray tubes, XFELs and Synchrotrons, the spectrum \mathcal{S} is well known. However, this does not hold true for laser-driven X-ray backlighter sources. The emitted spectrum is highly dependent on the backlighter target material and the laser intensity [15]. In general, the spectrum consists of bremsstrahlung [15] and backlighter material dependent fluorescence lines [28]. However, to our knowledge, the exact X-ray spectrum is unknown. Therefore, the grating setup is optimized using a monochromatic design energy. This energy is determined based on the

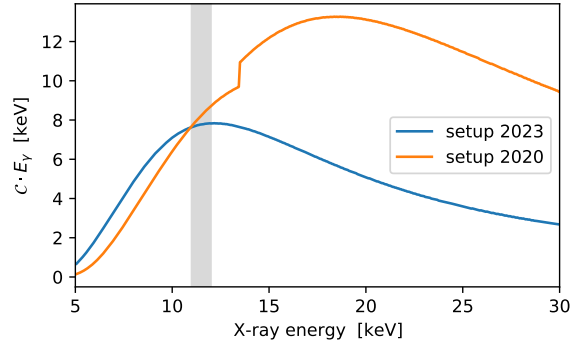


Figure 2. Comparison between the energy weighted detection efficiencies $C \cdot E_\gamma$ of the setup used in 2020 (orange curve) and the new setup for 2023 (blue curve). The gray vertical bar highlights the 11 to 12 keV region, which was found to be the dominant energy range for the setup in 2020 [10].

results of the experiment carried out in 2020 and on the energy-weighted detection efficiency $C \cdot E_\gamma$. The X-ray energy dependent detection efficiency C , is calculated via

$$C = T_{\text{Wafer } G_1} \cdot T_{\text{Wafer } G_2} \cdot T_{\text{Det. cover}} \cdot A_{\text{Det.}}, \quad (3.3)$$

with $T_{\text{Wafer } G_1}$ and $T_{\text{Wafer } G_2}$ the relative transmission of the grating wafers, $T_{\text{Det. cover}}$ the relative transmission of the X-ray detector cover and $A_{\text{Det.}}$ the absorption characteristic of the detector.

For the 2020 configuration, a dominant X-ray energy of about 11 to 12 keV was determined by Seifert et al. [40] and verified by Akstaller et al. in [10]. There, the imaging system was realized with two 500 μm thick polyimide wafers, an 8 μm aluminum foil, Fuji BAS type SR imaging plates and a 5 μm tungsten backlighter wire irradiated with about 30 J of laser energy in about 1 ps, distributed over a spot size with a diameter of about 5 μm .

For the new imaging setup, a detector, named Jungfrau detector, manufactured by the Paul Scherrer Institute (PSI) is used. This charge-integrating detector has a 320 μm thick silicon layer, and thus absorbs about 85% at 11 keV [41]. Using this detector is beneficial, since hardly any further noise originating from the detector is added to the acquired image [42]. Further, the spatial resolution is better compared to imaging plates [43, 44]. However, the Jungfrau detector will significantly change the X-ray energy dependent detection efficiency of the imaging system. Thus, the influence of the detector on the dominant imaging X-ray energy has to be evaluated.

The detection efficiencies C for both setups are calculated using equation (3.3) and with tabulated data taken from [41]. The curves in figure 2 show the product of C and E_γ , the energy weighted detection efficiency. For the 2020 setup (orange curve), the tender part of the energy range is suppressed by the absorbers in the beam path. The higher energies are suppressed a decline in X-ray absorption of the imaging plate. Note that it was assumed on the basis of Maddox et al. [44] that the absorption characteristic of the imaging plates is equivalent to its detection efficiency.

For the new imaging setups, the weighted detection efficiency function is plotted in blue. Beside the new Jungfrau detector, thinner wafers were used for the 2023 setup. The G_1 phase grating is manufactured on a 500 μm polyimide wafer and the G_2 on a 200 μm graphite substrate. Moreover, the aluminum foil is replaced with two 300 μm thick beryllium windows.

These windows are part of a shielding for the Jungfrau detector, which is protective against electromagnetic pulses (EMPs) [45]. This housing is necessary because the laser-matter interaction

generates strong EMPs in the GHz and THz regime of the electromagnetic spectrum [46], which corrupt the detector readout and make the images unusable.

Comparing the detection efficiencies in figure 2, it can be clearly seen that the spectral acceptance of the new setup 2023 is narrower compared to the setup of 2020. This is beneficial, since grating interferometers exhibit fringe visibility only in a confined energy range (see figure 6). With the new detector, the higher energies, which mainly contribute to the background signal and thus decrease the visibility of the fringe pattern, are suppressed. For the subsequent simulation of the grating interferometer, a design energy of 11 keV was chosen.

3.2 Imaged sample

As illustrated in figure 1, the imaged sample is a laser-driven blast wave in dense matter. To determine the required magnification and the minimal resolvable refraction angle α_{\min} , a simulated plasma shock is investigated. To obtain a number for the required relative improvement in the minimum detectable refraction angle compared to the previous experiment at the PHELIX laser in 2020, the simulated plasma shock is compared with data taken during that campaign.

The reference sample from 2020 is a $47 \times$ magnified $25 \times 1000 \mu\text{m}$ small polyimide foil, imaged edge-on view, see [10]. Figure 3(a) shows the simulated density distribution, integrated along the X-ray propagation direction, of this foil rotated by one degree. Source and detector blurring is incorporated by applying convolutions of the density profile with the shape of the source and the detector point spread function. With equation (2.5), the expected refraction angle $\Delta\alpha_{\text{obj}}$ is calculated for 11 and 12 keV. Due to the steep density gradient, the refraction angle reaches $120 \mu\text{rad}$ for 12 keV and about $145 \mu\text{rad}$ for 11 keV, see figure 3(b). The inset figure in the gray box in 3(b) shows the differential phase-contrast image $\Delta\varphi$ of the foil obtained in 2020. It can be seen that the differential phase-contrast signal of the foil is barely visible as vertical dark and bright stripes. The noise of the phase, i.e. $\text{std}(\Delta\varphi)$, is obviously large.

To generate realistic assumptions for the expected plasma in the 2023 campaign, 2D radiation-hydrodynamic simulations with MULTI [47] are performed with the parameters feasible at the PHELIX laser. The inset marked with a ③ on the top left in figure 1 shows the density distribution in a polycarbonat target, 5 ns after the onset of the PHELIX laser. This pulse was simulated with a duration of 1 ns and an intensity of $5 \cdot 10^{13} \text{Wcm}^{-2}$. Integrating the density distribution along the propagation direction of the X-rays results in the density profile plotted in figure 3(c). The small peak in the blue highlighted area at the right side is the plasma shock-front. The steady decrease of the density to the left side is caused by material ablation [48]. The resulting refraction angle is plotted in 3(d) for 10 and 11 keV. The refraction angles induced by the shock-front, reach about $16 \mu\text{rad}$ for 11 keV X-rays and $20 \mu\text{rad}$ for 12 keV X-rays.

Taking into account the maximum refraction angle of the simulated shock wave as the minimum value that should be observable, it is possible to calculate the required improvement of α_{\min} for the new setup. To get a signal from the plasma, as simulated for this particular case, with the same significance as the foil shown in the inset in figure 3(b), α_{\min} must be improved by a factor of at least 9. This value is used in section 4 to benchmark the improvement of the designed grating setup and to evaluate the reliability of the presented design concept.

The required magnification is determined only by the shock-front, highlighted in blue. This region is separately plotted in figure 3(e) and 3(f). When applying the moiré imaging technique, the

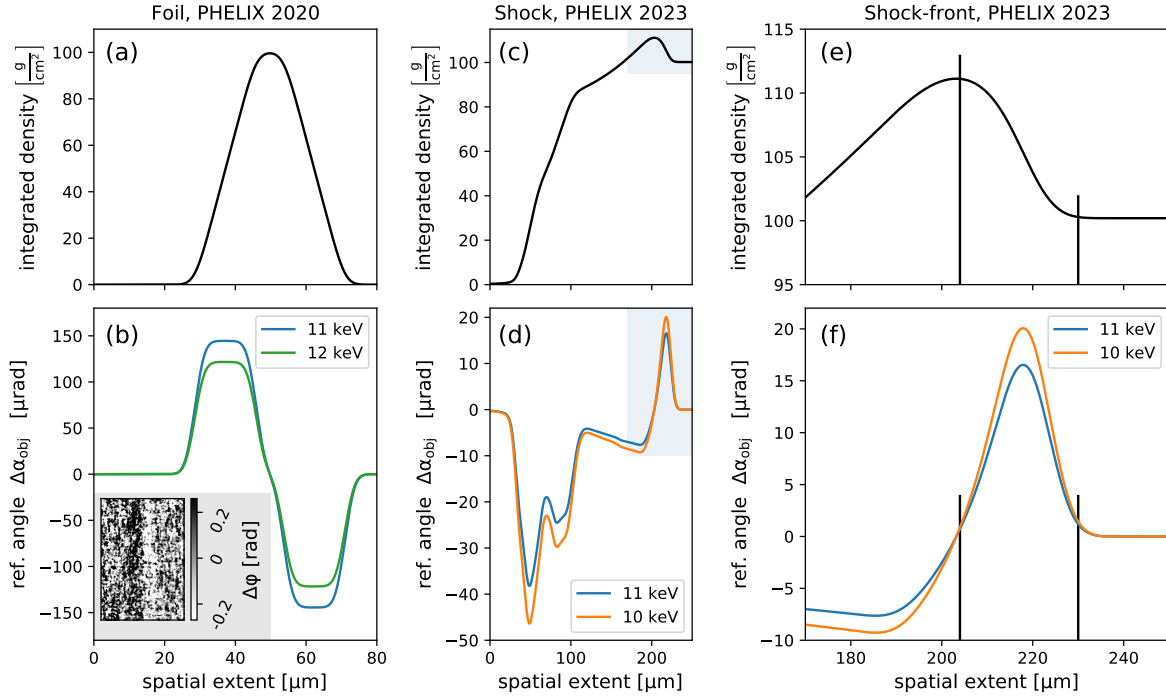


Figure 3. Overview of the imaged sample in 2020 at PHELIX (first column) and the sample for the campaign in 2023. (a) Integrated density profile of a tilted polyimide foil, imaged in 2020. (b) Calculated refraction angle for the foil at 11 keV (blue) and 12 keV (green). The inset shows the reconstructed DPC image (data taken from [10]). (c) Integrated density profile of the simulated shock in the X-ray propagation direction is shown in figure 1. The blue marked area at the top left is the shock-front and printed enlarged in (e). The refraction angles, induced by the plasma shock is shown in (d) for 11 keV in blue and 10 keV in orange. The zoom into the shock-front is depicted in (f). The vertical black lines indicate the spatial extent of the positive gradient of the shock-front.

differential phase-contrast signal cannot be retrieved individually for every pixel. The pattern used for retrieving the phase-shift are the moiré fringes, which extend to about seven pixels per period [31]. Thus, we aim for a magnification such that the peak in the refractive angle is covered by at least one period. With the spatial extent of $26 \mu\text{m}$, and a moiré period of $350 \mu\text{m}$, the required magnification of the object into the detector should be at least 14.

3.3 Geometric and experimental constraints

To meet the derived requirements, the spatial arrangement of the imaged sample and the detector must be considered. Since equation (2.6) for the minimum observable refraction angle α_{\min} incorporates only the magnification of the object into the G_1 grating, a larger distance between the source and the detector does not affect the minimal detectable refractive angle but increases the object magnification. However, increasing the distance between the source and the detector will decrease the number of photons per detector pixel, and thus will increase the photon noise. Furthermore, if the distance between the source and object is increased, less photons contribute to the signal of the sample.

Beside these theoretical aspects, experimental constraints must be taken into account. The electromagnetic pulse protective housing for the Jungfrau detector must fit in the [experimental](#)

chamber of the PHELIX laser. Due to the technical realization of the EMP protective box for the detector, the minimal distance between the G_2 grating and the detector is about 300 mm. The detector was placed at 900 mm in the simulations, the longest conceivable distance $d(S, \text{Det.})$ in the PHELIX target chamber. As the initial position of the sample, 30 mm is chosen. The realized magnification is 30 and thus more than required. Further, the small distance to the source increases the photon flux through the object.

3.4 Optimization parameter and numerical simulation

In section 3.2, a lower limit for the required improvement of the minimal detectable refractive angle α_{\min} was determined. The same concept is applied for the simulations and a relative improvement factor ξ is introduced, which is calculated via

$$\xi = \frac{\alpha_{\min, 20}}{\alpha_{\min}}, \quad (3.4)$$

with the minimal detectable refractive angle $\alpha_{\min, 20}$ for the setup 2020 and α_{\min} for the setup 2023. Inserting and rearranging equation (2.6) and (2.7) into (3.4) results in

$$\xi = \frac{P_{G_2, 20}}{P_{G_2}} \frac{M_{(\text{Obj}, G_1), 20}}{\frac{d(Q, G_1)}{d(Q, \text{Obj})}} \frac{d(G_1, G_2)}{d(G_1, G_2)_{20}} \frac{V}{V_{20}} \sqrt{\frac{N}{N_{20}}}, \quad (3.5)$$

with P_{G_2} the G_2 grating period, $M_{(\text{Obj}, G_1)}$ the magnification of the object into the G_1 grating, $d(G_1, G_2)$ the inter-grating distance, V the fringe visibility and N the number of photons per pixel each with the index 20 for the respective values for the setup 2020. Since the number of photons is unknown, the relative change in number of photons can be expressed via

$$\frac{N}{N_{20}} = \frac{1 - \text{DC}_{G_2}}{1 - \text{DC}_{G_2, 20}} \frac{A_{\text{Pix}}}{A_{\text{Pix}, 20}} \left(\frac{d(Q, \text{Det})_{20}}{d(Q, \text{Det})} \right)^2, \quad (3.6)$$

with DC_{G_2} the duty cycle of the G_2 grating, A_{Pix} the area of one pixel and $d(Q, \text{Det})$ the total length of the setup. All variables given in equations (3.5) and (3.6) were either determined in the previous section, or are varied during the simulation.

The simulation is based on the scalar diffraction theory [1] and follows the implementation given in Ritter et al. [49]. The simulation uses a wave field propagation through space with the band-limited angular spectrum method described in [50]. The transmission through objects is implemented using the projection approximation [1]. The required material constants for the calculation are taken from [51]. Source and detector blurring are taken into account by convolving the magnified source spot and the detector point spread function [43] with the simulated image. The moiré pattern is generated by superimposing the G_2 grating with a slightly different period than the magnified Talbot pattern. The visibility of the pattern is determined using equation (2.1).

To determine the optimal grating setup, DC_{G_2} is varied between 0.48 and 0.77 in steps of 0.15, P_{G_1} between 8.2 and 13 μm in 0.2 μm steps, $d(Q, G_1)$ between 0.14 and 0.42 m and $d(G_1, G_2)$ between 0.10 and 0.50 m in 0.01 m steps. The height of the G_1 grating was chosen to be optimal π -shifting for 11 keV and a duty cycle of 0.5. During simulation, the period of G_2 is calculated to produce a seven-pixel-per-period moiré pattern.

In the top row of figure 4, three 2D-maps are plotted to show the simulation results. On the horizontal axis the G_2 duty cycle DC_{G_2} and on the vertical axis the G_1 period P_{G_1} is varied for given

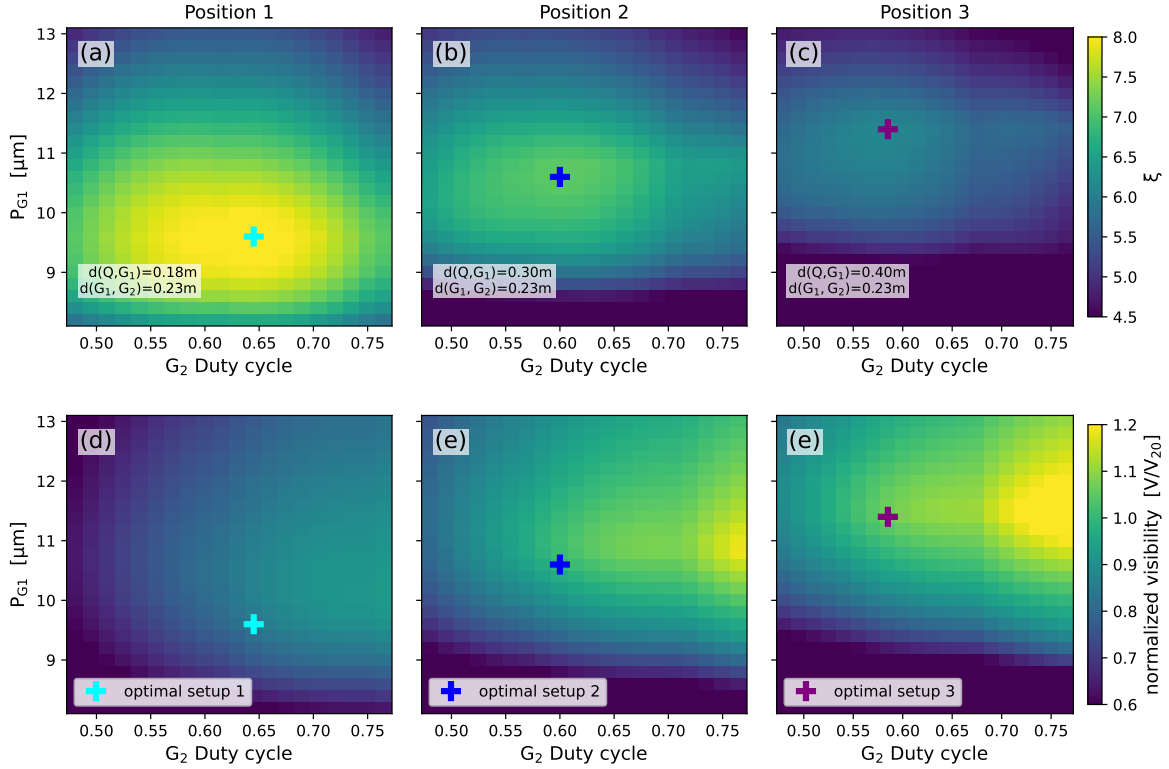


Figure 4. Simulated results for three different grating geometries, depending on the choice of the G_1 period and the G_2 Duty cycle. The positions of G_1 and G_2 are given in the legend. *Top row:* relative improvement of α_{\min} , ξ , the coloured crosses mark the maximum achievable improvement for the given set of parameters. *Bottom row:* corresponding visibility maps of the same geometry given in the plot above.

grating positions $d(Q, G_1)$ and $d(G_1, G_2)$. The color code depicts the values of ξ . The distance $d(Q, G_1)$ increases from 0.18 m for plot 4(a) to 0.30 m for 4(b) to 0.40 m for 4(c), while $d(G_1, G_2)$ is kept constant at 0.23 m. The crosses mark the combination of duty cycle and period, that gives the highest improvement. These positions are subsequently referred to as optimal setups. The largest improvement of α_{\min} is reached with the compact configuration. However, since the simulation neglects all sources of noise, the change in visibility should be additionally considered individually. Therefore, in the bottom row of figure 4, the associated visibility maps, normalized with the simulated visibility of the 2020 setup, are plotted in the same way. The compact configuration suffers a significant loss of visibility; the larger ones give a comparable result.

The maximum values of ξ for every simulated G_1 and G_2 position combination are arranged regarding their G_1 and G_2 positions to generate a 2D-map. This map is shown in figure 5(a) and visualizes the highest achievable relative improvements of ξ , for a given position of G_1 and G_2 . The three crosses mark the positions investigated in figure 4. The plot in figure 5(b) depicts the change of the visibility for the selected grating parameters that give the optimal value of ξ . On the right side of the figure, the required G_1 period P_{G_1} 5(c), G_2 Duty cycle DC_{G_2} 5(d) and G_2 period P_{G_2} 5(e) is plotted.

The 2D-map of ξ shows that the relative improvement has a wide maximum with values of about 8. For larger distances $d(G_1, G_2)$, this value does not change, which is counter-intuitive when considering equation (2.6). It seems, that the improvement from the larger inter-grating distance gets

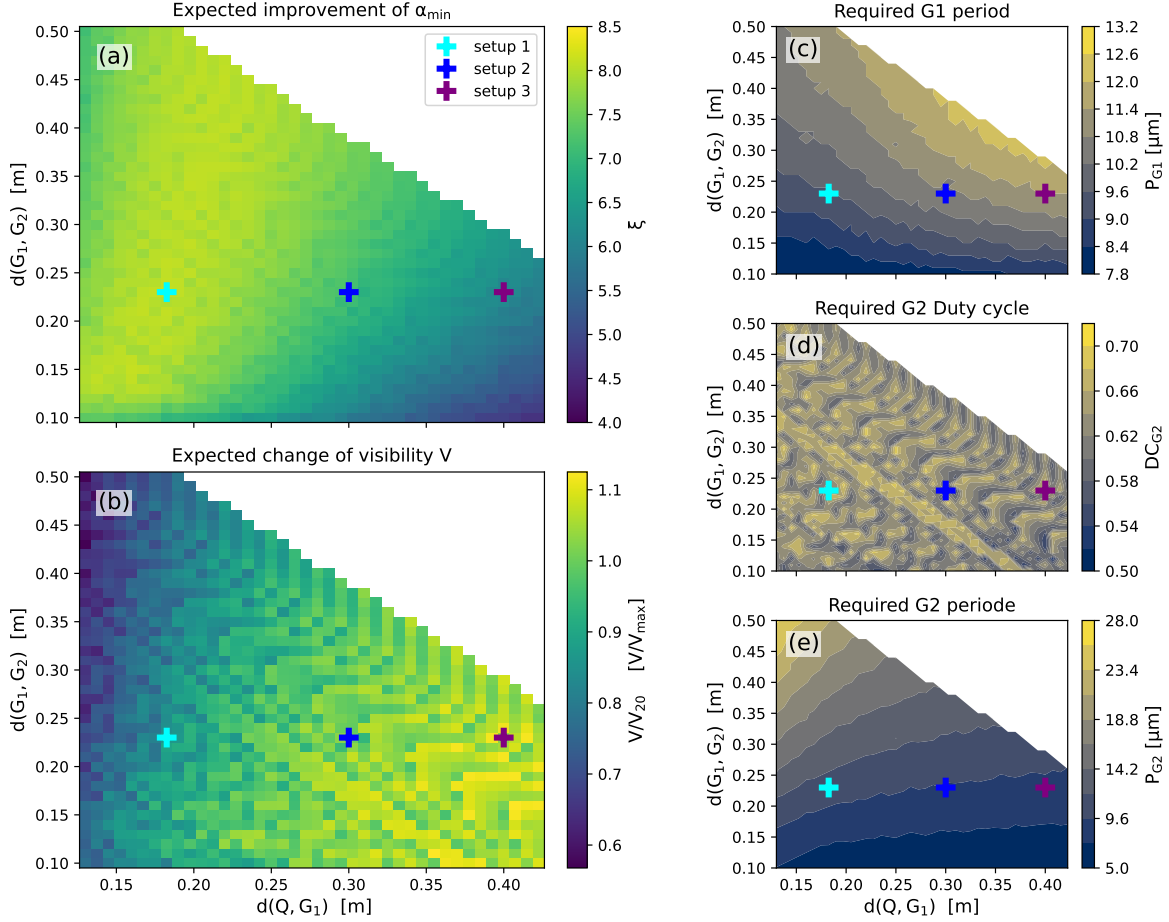


Figure 5. Final results gained from the simulation. In (a) the expected improvement of α_{\min} is plotted as a function of $d(Q, G_1)$ and $d(G_1, G_2)$. The coloured crosses mark the position of the setups investigated in figure 4. The associated grating parameters found via the optimization process are plotted on the right side. (c) shows the required G_1 period, (d) the duty cycle of G_2 and (e) the required G_2 period. The expected change in visibility relative to 2020, with the parameters given in the right column, is shown in (b).

counteracted with the required larger G_2 grating periods, see plot 5(e). By looking at the plot 5(b), a noticeable decrease in the visibility is observable for short distances $d(Q, G_1)$ and long distances $d(G_1, G_2)$. This is caused by the source blurring. Since the visibility in 2020 was about 15%, a significant reduction in visibility for the new setup should be avoided.

Thus, before selecting a grating setup, its robustness is investigated. For this purpose, the three setups marked in figure 5, are benchmarked further. First, the effect of a larger spot size onto ξ is investigated. This is important, since the spot size from laser-driven X-ray backlighter can vary from shot to shot [52]. Therefore, the simulation is performed with varying spot sizes from 1 μm to 15 μm . The results are plotted in figure 6. The black vertical line at 5 μm marks the source size expected from a 5 μm backlighter wire. As expected, the minimal detectable refractive angle tends to decrease for larger spot sizes, since the Talbot pattern is increasingly smeared out, which results in a smaller moiré visibility. In agreement to previous findings, setup 1 exhibits the highest values for ξ . However, the gradient with which ξ decreases differs for all three setups. If the source size is only 1 μm larger than the assumed 5 μm , setup 2 and setup 1 perform comparable.

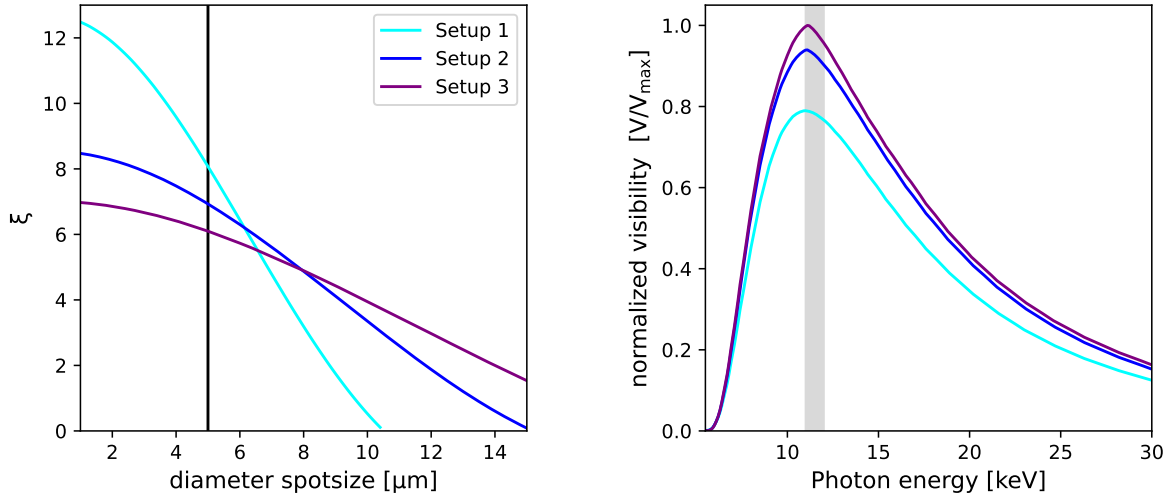


Figure 6. Robustness test of three selected setups. The position of these are marked in figure 5. *Left:* influence of the X-ray spot diameter onto ξ , the achievable relative improvement of α_{\min} . The black vertical line marks 5 μm , the expected and simulated spot size of the X-ray backlighter. *Right:* function of the photon energy dependent visibility of the three setups. The values are normalized with the maximal visibility value of setup 3. The gray vertical bar highlights the 11 to 12 keV region.

A further test is the variation of the photon energy, which gives an insight into the spectral response of the setup. The right plot in figure 6 shows the energy dependency of the moiré visibility. The values are normalized with the maximum reachable visibility values of setup 3. The gray vertical bar in the plot shows the 11 to 12 keV range. As expected, all three setups reach the highest fringe contrast at the design energy of 11 keV and exhibit lower contrast for lower and higher energetic X-rays. Due to the fact that the maximum is relatively broad, the setups will still perform well, even if the weighted mean X-ray energy of the new setup changes due to the digital detector.

For the final selection of the grating parameters, all simulated data is taken into account. After considering possible advantages and disadvantages of a grating setup which is either robust like setup 3, or is tuned to the limit (setup 1), we have opted for a compromise by choosing the intermediate configuration. Thus, we decided to use a configuration similar to setup 2. The gratings were produced by the Institute of Microstructure Technology (IMT/KIT) using the deep X-ray lithography process [53]. The grating parameters are presented in table 1.

Table 1. Parameters of the manufactured gratings, which were produced on the basis of the simulation studies. The grating height of G_1 is π -shifting for 11 keV.

	Period [μm]	Material	height [μm]	duty cycle	d(S, Grating) [m]
G_1	10.6	Polyimide	30	0.5	0.30
G_2	9.5	Gold	95	0.58 – 0.6	0.538

The expected visibility is about the same as in 2020. Further, the setup is robust regarding a fluctuation in the X-ray spot size. However, compared to setup 1, the expected improvement of α_{\min} is about 10% lower with 7.1. Thus, the derived threshold of 9 for ξ , which was derived in section 3.2,

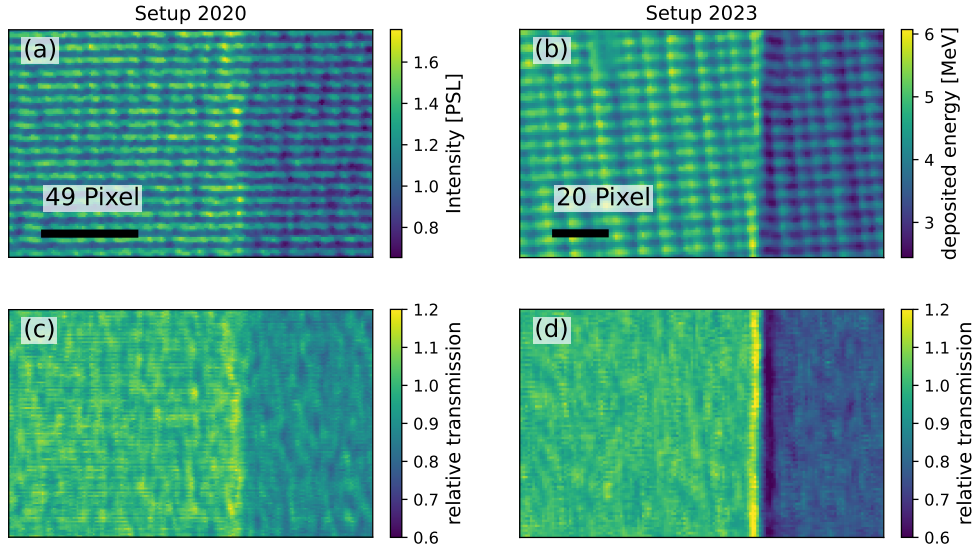


Figure 7. *Top row:* raw detector images of a vertically arranged PMMA edge acquired in 2020 (a) and in 2023 (b), smoothed with a 3×3 median filter. In 2020 the object thickness was 1 mm and 0.5 mm in 2023. The intensity is given for the 2020 setup in photostimulated luminescence (PSL) units [44] and for the setup 2023 in deposited energy in MeV. The moiré pattern was adjusted to a period of 7 pixels in (a) and 6.5 in (b) using the method described in [9]. The black scale indicates $50 \mu\text{m}$ in the object plane. Due to the different magnification and pixel size, the effective pixel size in the object plane differs significantly. *Bottom row:* reconstructed transmission images generated with the respective object measurement above.

could not be met with the assumptions made. However, there are expected improvements in image quality which have not been considered yet. First, according to [11], the noise in the differential phase-contrast image can be reduced by about 13% when using multiple reference images for the reconstruction. Applying this technique would increase the improvement ξ to 8.1. Further, the Jungfrau detector adds, compared to imaging plates, less noise to the acquired image. To the best of our knowledge, there is no publication available that compares these types of detectors. Hence, estimating a number for potential improvements is difficult and therefore omitted.

4 Experimental verification of the design process at the PHELIX laser

For an experimental benchmark, data acquired at the PHELIX laser with the optimized setup is compared with data from 2020. To this end, the retrieved transmission and differential phase-contrast images are compared at first qualitatively, followed by a quantitative analysis.

Detector images of object measurement are shown in the top row of figure 7; on the left side, the data from 2020, on the right side, from 2023. Both targets are sheets of PMMA with a respective thickness of 1 mm in 2020 and 0.5 mm in 2023. The sheet is positioned vertically at the right side of the image. These images are used in combination with a reference image to reconstruct the transmission and the differential phase-contrast image modality. To ensure a valid comparison, the same reconstruction algorithm and corrections are applied.

The reconstructed transmission images are shown in the lower row of figure 7. Although a thinner sample was probed in 2023, the image shows a higher absorption contrast than the 2020 image. This

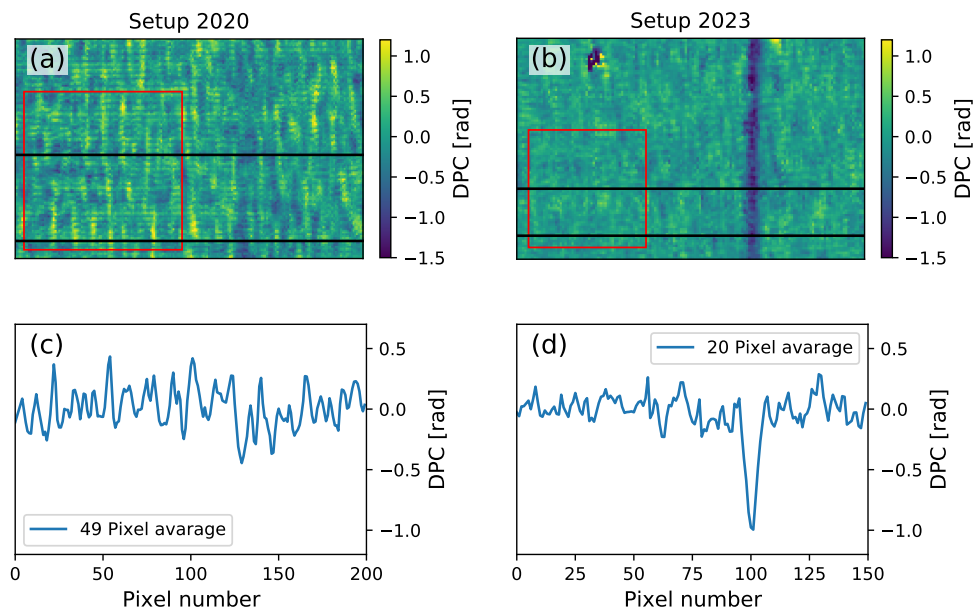


Figure 8. *Top row:* reconstructed differential phase-contrast images generated with the object measurement shown in figure 7. In image (a) the edge is barely visible, whereas in (b) the edge is clearly visible as a dark vertical bar. The red frame marks the area which is used to determine the standard deviation of the DPC signal. Note that the noisy spot at the top left of the image (b) is caused by a defect in the G_1 grating, which was caused by laser ablated material impinging onto the grating surface. The plots in the *bottom row* show the averaged line outs from the region marked by the black horizontal lines in the images above.

result can be explained by the weighted detection efficiencies (see figure 2) and highlights the advantage of the Jungfrau detector being less sensitive in the high-energy part of the X-ray spectrum compared to image plates. Further, a pronounced propagation-based phase-contrast signal is visible along the PMMA edge in the image of 2023. Since this publication is focused on grating-based phase-contrast imaging, the transmission image modality is not discussed any further. A detailed analysis of a static test sample imaged with propagation-based phase-contrast at the PHELIX laser can be found in [10].

The differential phase-contrast images are presented in the top row of figure 8. As the direction of X-ray propagation is not parallel to the edge of the PMMA target, the edge is effectively a steep wedge. This density gradient can be seen as negative differential phase-contrast values and is clearly visible in image 8(b), generated with the new setup. In contrast to this, the DPC signal of the edge is only faintly visible in image 8(a). To evaluate this finding in more detail, the DPC images are averaged within the region marked with the black lines. This region is equivalent to $50\ \mu\text{m}$ in the object plane for both setups, which accounts for the effect of the different magnification. Still, the PMMA edge cannot be distinguished from the noise in the line-out from the DPC image acquired with the setup 2020. In contrast to that, the edge exhibits significantly larger DPC values for the image acquired with the setup from 2023 and is clearly visible. The noise in the free-field is evaluated for both images within the red rectangle. For this, the values are plotted as a histogram and a Gaussian distribution is fitted. For image 8(a), the standard deviation $\text{std}(\Delta\varphi)$ is 0.33 and 0.17 for image 8(b).

For the quantitative evaluation of the gained improvement of the minimal detectable refractive angle, the definition of α_{\min} and the optimization parameter ξ are used. Inserting equation (2.6)

into equation (3.4) results in

$$\xi = \underbrace{\frac{P_{G_2}^{20} \cdot M_{(\text{Obj}, G_1)}^{20}}{d (G_1 G_2)^{20}} \bigg/ \frac{P_{G_2}^{23} \cdot M_{(\text{Obj}, G_1)}^{23}}{d (G_1 G_2)^{23}}}_{\text{phase sensitivity term}} \cdot \underbrace{\frac{\text{std}(\Delta\varphi)^{20}}{\text{std}(\Delta\varphi)^{23}}}_{\text{noise term}} = 7.4 \quad (4.1)$$

with the inter-grating distance $d(G_1, G_2)$, P_{G_2} the period of G_2 , $M_{(\text{Obj}, G_1)}$ the magnification of the object into the G_1 plane and $\text{std}(\Delta\varphi)$ and the standard deviation of the differential phase-contrast image. The indices 20 and 23 indicate the associated setups. The expected improvement ξ can be separated into a phase sensitivity term and a noise related term. The phase sensitivity term consists only of values that can be measured with high accuracy and can therefore be considered to be predictable with negligible uncertainty. Inserting the numbers, given in table 1 for the setup 2023 and in [10] for the 2020 setup, the phase sensitivity term is improved by a factor of 3.7. This means that the signal visible in the DPC image will be 3.7 times higher for the 2023 setup than for the 2020 setup when imaging the same object. With this factor, the larger DPC signal in figure 8 for the new setup can be understood. The noise related term in equation (4.1) incorporates the photon flux and the fringe visibility which were estimated in the simulation. Therefore, this term may differ from the simulated expectation. With the previously determined values for $\text{std}(\Delta\varphi)$, the standard deviations in the DPC images, the noise term is 2.0. This means that the noise in the DPC has been reduced by a factor of two, resulting in a lower threshold for a significant signal in the DPC image. The total improvement of the minimal detectable refraction angle is $\xi = 7.4$. In section 3.2 it was stated that the required improvement in the minimum detectable angle of refraction to resolve the simulated plasma shown in figure 1 was $\xi = 9$. This value could not be achieved by optimizing the imaging setup alone. By applying the multiple reference frame noise reduction method [11], the improvement of the minimal detectable refraction angle ξ can be further increased. An additional gain of ξ could be achieved by using a probe-laser with higher energy. The higher energy implies a higher photon flux and thus, according to equation (2.7), a lower noise in the differential phase contrast image. Further, it should be noted that the required factor ξ is highly dependent on the investigated object. For example, if a stronger pump laser is used, a larger shock with higher compression can be expected, inducing larger angles of refraction. Subsequently, less improvement of α_{\min} would be already sufficient to generate a significant signal in the differential phase contrast image.

The simulated improvement for the chosen setup 2 in section 3.4 was about $\xi = 7.1$. This is in very good agreement with the experimental result of $\xi = 7.4$. This indicates that the noise term was correctly estimated. However, one could argue that the experimental improvement could also be influenced by parameters outside the range of parameters considered in the current version of this optimization process. For example, the noise characteristic of the detectors used were not incorporated. Further, the simulation was performed monochromatically, omitting the effect of the spectrum. However, by incorporating experimental data from 2020 into the optimization process, the effect of these unknown parameters has been minimized, thus implying that a good agreement between simulation and experiment can be expected. Hence, this fairly good agreement of prediction and experiment shows that the assumptions made are valid and can be used to reliably optimize a setup for high phase sensitivity. For the presented grating setup the minimal detectable refraction angle α_{\min} is, following equation (2.6), about 10 μrad .

5 Conclusion and outlook

A design process for a highly phase-sensitive two-grating Talbot-interferometer is presented. The optimization of the interferometer is performed with respect to the minimal detectable refraction angle. Since this interferometer is designed for a pump-probe experiment with a laser driven X-ray source, the photon flux and the visibility is incorporated in the optimization procedure as only single-shot acquisition with a limited number of photons is possible. The predicted performance of the grating interferometer is with a minimal detectable refraction angle α_{\min} of 10 μrad , in fairly good agreement with the experimental data.

With a known spectrum, the presented design approach can also be used to optimize a grating setup for different backlighter materials that have their fluorescence lines at lower X-ray energies. This can be beneficial for imaging laser-driven shock waves in low-density foams, since the expected density gradients are smaller which could be partially compensated with higher values of the X-ray energy dependent refractive index decrement δ . Further, with slight modifications, the approach can be also used for optimizing a Talbot interferometer for common laboratory X-ray transmission microfocus tubes. In that way, this paper provides a flexible and well documented method for optimizing a Talbot interferometer with respect to the minimal detectable refraction angle.

Acknowledgments

The results presented here are based on the experiments P-21-00013 and P186, which were performed at the PHELIX facility at the GSI Helmholtzzentrum für Schwerionenforschung, Darmstadt (Germany) in the frame of FAIR Phase-0. We would like to give special thanks to the PHELIX operation team.

The authors acknowledge the support of the Karlsruhe Nano Micro Facility (KNMF), a Helmholtz Research Infrastructure at Karlsruhe Institute of Technology, and microworks GmbH for fabricating the gratings.

This work was funded by the Deutsche Forschungsgemeinschaft (DFG) within the [grant number 452935060](#). The work of A.S. Martynenko was supported by the Alexander von Humboldt Foundation.

References

- [1] D. Paganin, *Coherent X-Ray Optics*, Oxford University Press (2006) [[DOI:10.1093/acprof:oso/9780198567288.001.0001](#)].
- [2] D. Stutman and M. Finkenthal, *Talbot-Lau X-ray interferometry for high energy density plasma diagnostic*, *Rev. Sci. Instrum.* **82** (2011) 113508.
- [3] G. Anton et al., *Grating-based darkfield imaging of human breast tissue*, *Z. Med. Phys.* **23** (2013) 228.
- [4] V. Ludwig et al., *Exploration of different X-ray Talbot-Lau setups for dark-field lung imaging examined in a porcine lung*, *Phys. Med. Biol.* **64** (2019) 065013.
- [5] M. Viermetz et al., *Initial Characterization of Dark-Field CT on a Clinical Gantry*, *IEEE Trans. Med. Imaging* **42** (2023) 1035.
- [6] V. Revol, B. Plank, R. Kaufmann, J. Kastner, C. Kottler and A. Neels, *Laminate fibre structure characterisation of carbon fibre-reinforced polymers by X-ray scatter dark field imaging with a grating interferometer*, *NDT Int.* **58** (2013) 64.

- [7] V. Ludwig et al., *A phase-sampling method for an X-ray Talbot-Lau scanner with continuous grating movement*, *2020 JINST* **15** P01010.
- [8] L. Antonelli et al., *X-ray phase-contrast imaging for laser-induced shock waves*, *Europhys. Lett.* **125** (2019) 35002.
- [9] M. Schuster et al., *A fast alignment method for grating-based X-ray phase-contrast imaging systems*, *2019 JINST* **14** P08003.
- [10] B. Akstaller et al., *Single-shot grating-based phase-contrast imaging of a micrometer sample at a laser-driven X-ray backlighter source*, *2021 JINST* **16** P06021.
- [11] S. Schreiner et al., *Noise Reduction for Single-Shot Grating-Based Phase-Contrast Imaging at an X-ray Backlighter*, *J. Imaging* **7** (2021) 178.
- [12] M.P. Valdivia et al., *Talbot-Lau X-ray deflectometer: Refraction-based HEDP imaging diagnostic*, *Rev. Sci. Instrum.* **92** (2021) 065110.
- [13] G. Pérez-Callejo et al., *Phase imaging of irradiated foils at the OMEGA EP facility using phase-stepping X-ray Talbot-Lau deflectometry*, *High Power Laser Sci. Eng.* **11** (2023) e49.
- [14] V. Bagnoud et al., *Commissioning and early experiments of the PHELIX facility*, *Appl. Phys. B* **100** (2010) 137.
- [15] B. Borm, D. Khaghani and P. Neumayer, *Properties of laser-driven hard X-ray sources over a wide range of laser intensities*, *Phys. Plasmas* **26** (2019) 023109.
- [16] D.S. Montgomery, *Invited article: X-ray phase contrast imaging in inertial confinement fusion and high energy density research*, *Rev. Sci. Instrum.* **94** (2023) 021103.
- [17] P. Modregger, B. Pinzer, T. Thüring, S. Rutishauser, C. David and M. Stampanoni, *Sensitivity of X-ray grating interferometry*, *Opt. Express* **19** (2011) 18324.
- [18] J. Rieger et al., *Optimization procedure for a Talbot-Lau X-ray phase-contrast imaging system*, *2017 JINST* **12** P04018.
- [19] T. Weitkamp, I. Zanette, F. Pfeiffer and C. David, *Design aspects of X-ray grating interferometry*, in the proceedings of the *International Workshop on X-Ray and Neutron Phase Imaging with Gratings*, Tokyo, Japan, 5–7 March 2012, American Institute of Physics (2012) [*AIP Conf. Proc.* **1466** (2012) 84].
- [20] T. Thüering and M. Stampanoni, *Performance and optimization of X-ray grating interferometry*, *Philos. Trans. Roy. Soc. Lond. A* **372** (2014) 20130027.
- [21] T. Weitkamp et al., *X-ray phase imaging with a grating interferometer*, *Opt. Express* **13** (2005) 6296.
- [22] F. Pfeiffer, T. Weitkamp, O. Bunk and C. David, *Phase retrieval and differential phase-contrast imaging with low-brilliance X-ray sources*, *Nat. Phys.* **2** (2006) 258.
- [23] N. Bevins, J. Zambelli, K. Li, Z. Qi and G.-H. Chen, *Multicontrast X-ray computed tomography imaging using Talbot-Lau interferometry without phase stepping: single-shot phase contrast CT*, *Med. Phys.* **39** (2011) 424.
- [24] M. Takeda, H. Ina and S. Kobayashi, *Fourier-transform method of fringe-pattern analysis for computer-based topography and interferometry*, *J. Opt. Soc. Am.* **72** (1982) 156.
- [25] T.J. Suleski, *Generation of Lohmann images from binary-phase Talbot array illuminators*, *Appl. Opt.* **36** (1997) 4686.
- [26] C. David, B. Nöhammer, H.H. Solak and E. Ziegler, *Differential X-ray phase contrast imaging using a shearing interferometer*, *Appl. Phys. Lett.* **81** (2002) 3287.

- [27] A. Momose, S. Kawamoto, I. Koyama, Y. Hamaishi, K. Takai and Y. Suzuki, *Demonstration of X-Ray Talbot Interferometry*, *Jpn. J. Appl. Phys.* **42** (2003) L866.
- [28] H.-S. Park et al., *High-energy $K\alpha$ radiography using high-intensity, short-pulse lasers*, *Phys. Plasmas* **13** (2006) 056309.
- [29] H.F. Talbot, *LXXVI. Facts relating to optical science. No. IV*, *Lond. Edinb. Dubl. Phil. Mag. J. Sci.* **9** (1836) 401.
- [30] *The Theory of the Moiré Phenomenon*, Springer, London, U.K. (2009) [DOI:10.1007/978-1-84882-181-1].
- [31] M. Seifert et al., *Improved Reconstruction Technique for Moiré Imaging Using an X-Ray Phase-Contrast Talbot-Lau Interferometer*, *J. Imaging* **4** (2018) 62.
- [32] E.E. Bennett, R. Kopace, A.F. Stein and H. Wen, *A grating-based single-shot X-ray phase contrast and diffraction method for in vivo imaging*, *Med. Phys.* **37** (2010) 6047.
- [33] F. Pfeiffer et al., *Hard-X-ray dark-field imaging using a grating interferometer*, *Nat. Mater.* **7** (2008) 134.
- [34] T. Michel et al., *On a dark-field signal generated by micrometer-sized calcifications in phase-contrast mammography*, *Phys. Med. Biol.* **58** (2013) 2713.
- [35] M. Engelhardt et al., *High-resolution differential phase contrast imaging using a magnifying projection geometry with a microfocus X-ray source*, *Appl. Phys. Lett.* **90** (2007) 224101.
- [36] K.J. Engel et al., *Contrast-to-noise in X-ray differential phase contrast imaging*, *Nucl. Instrum. Meth. A* **648** (2011) S202.
- [37] T. Weber et al., *Noise in X-ray grating-based phase-contrast imaging*, *Med. Phys.* **38** (2011) 4133.
- [38] A. Wolf, *X-ray microscopy and phase imaging towards time-resolved applications in laboratory astrophysics*, Doctoral Thesis, Friedrich-Alexander-Universität Erlangen-Nürnberg (FAU) (2022).
- [39] A. Schropp et al., *Imaging Shock Waves in Diamond with Both High Temporal and Spatial Resolution at an XFEL*, *Sci. Rep.* **5** (2015) 11089.
- [40] M. Seifert et al., *Evaluation of the Weighted Mean X-ray Energy for an Imaging System Via Propagation-Based Phase-Contrast Imaging*, *J. Imaging* **6** (2020) 63.
- [41] B.L. Henke, E.M. Gullikson and J.C. Davis, *X-Ray Interactions: Photoabsorption, Scattering, Transmission, and Reflection at $E = 50$ -30,000 eV, $Z = 1$ -92*, *At. Data Nucl. Data Tables* **54** (1993) 181.
- [42] A. Mozzanica et al., *Characterization results of the JUNGFRÄU full scale readout ASIC*, 2016 *JINST* **11** C02047.
- [43] J.H. Jungmann-Smith et al., *JUNGFRÄU 0.2: prototype characterization of a gain-switching, high dynamic range imaging system for photon science at SwissFEL and synchrotrons*, 2014 *JINST* **9** P12013.
- [44] B.R. Maddox et al., *High-energy X-ray backlighter spectrum measurements using calibrated image plates*, *Rev. Sci. Instrum.* **82** (2011) 023111.
- [45] S. Schreiner et al., *Electromagnetic pulse protective shielding for digital X-ray detectors*, *Rev. Sci. Instrum.* **94** (2023) 075106.
- [46] F. Consoli et al., *Laser produced electromagnetic pulses: generation, detection and mitigation*, *High Power Laser Sci. Eng.* **8** (2020) e22.
- [47] R. Ramis, J. Meyer-ter-Vehn and J. Ramírez, *MULTI2D — a computer code for two-dimensional radiation hydrodynamics*, *Comput. Phys. Commun.* **180** (2009) 977.

- [48] P. Mulser and D. Bauer, *High Power Laser-Matter Interaction*, Springer (2010) [DOI:10.1007/978-3-540-46065-7].
- [49] A. Ritter et al., *Simulation of dark-field imaging of micro-calcifications in human breast tissue with X-ray Talbot-Lau interferometry*, 2014 JINST **9** C05028.
- [50] K. Matsushima and T. Shimobaba, *Band-limited angular spectrum method for numerical simulation of free-space propagation in far and near fields*, *Opt. Express* **17** (2009) 19662.
- [51] C.T. Chantler, K.J. Olsen, R.A. Dragoset, A.R. Kishore, S.A. Kotochigova and D.S. Zucker, *X-Ray Form Factor, Attenuation, and Scattering Tables*, version 2.0, National Institute of Standards and Technology, Gaithersburg, MD, U.S.A. (2003) [DOI:10.18434/T4HS32].
- [52] E. Brambrink et al., *Short-pulse laser-driven X-ray radiography*, *High Power Laser Sci. Eng.* **4** (2016) e30.
- [53] P. Meyer, T. Beckenbach, F. An, T. Schröter, J. Schulz and J. Mohr, *X-ray gratings for grating-based X-ray dpci fabricated using the deep X-ray lithography process: State of the art*, in the proceedings of the 4th International conference on X-ray and Neutron Phase Imaging with Gratings (XNPIG2017), Zurich, Switzerland, 12–15 September 2017, pp. 110–111 [DOI:10.13140/RG.2.2.27923.37922].